Effect of micro-architectural design and polymer infiltration on mechanical properties and fatigue life of strut- and sheet-based lattice bone scaffolds

Niar, S. Kazemivand; Nikaein, G.; Sadeghi, M. H.; Vrancken, B.; van Hooreweder, B.; Mirzaali, M. J.

Important note
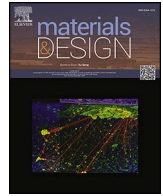To cite this publication, please use the final published version (if applicable).
Please check the document version above.

Effect of micro-architectural design and polymer infiltration on mechanical properties and fatigue life of strut- and sheet-based lattice bone scaffolds

S.Kazemivand Niar [a], G. Nikaein [a], M.H. Sadeghi [a],[*] , B. Vrancken [c], B. van Hooreweder [c], M.J. Mirzaali [b]

[a] Faculty of Mechanical Engineering, Tarbiat Modares University, Tehran, Iran
[b] Department of Biomechanical Engineering, Faculty of Mechanical, Maritime, and Materials Engineering, Delft University of Technology (TU Delft), Mekelweg 2, 2628 CD Delft, the Netherlands
[c] Deparment of Mechanical Engineering, Katholieke Universiteit Leuven, Leuven, Belgium

ABSTRACT

Lattice structures are widely used in biomedical engineering, primarily due to their exceptional properties which results from their unique microstructural features. The variability in geometric parameters of the lattice microstructure, enables property adjustment to meet different needs. In this paper, the mechanical properties of lattice structures are investigated with respect to unit cell type, porosity, and presence of an infiltrated resin, which simulates bone tissue within the scaffold. Digital image correlation technique was employed to assess deformation modes in in-filled structures. Three different architectures, including Diamond, FCC and Gyroid with three distinct relative densities of 15 %, 25 %, and 35 % have been designed and fabricated using Ti-6Al-4 V biomaterial. Results showed that the Gyroid lattice structures demonstrated superior mechanical properties compared to Diamond and FCC lattices under quasi-static compression tests. Distinct failure behavior was also observed across the structures. At higher relative densities, Diamond and FCC lattices formed 45° macro-cracks, whereas Gyroid samples compressed severely without macro-cracks. Furthermore, in-filled structures, demonstrated up to 1.3 times higher strength compared to their as-built counterparts. Notably, a unified master curve was developed to facilitate the prediction of fatigue lives of all geometries. These findings support the development of implants with enhanced longevity and performance.

1. Introduction

Over the past two decades, significant progress has been made in the fabrication of metallic biomaterials through additive manufacturing (AM), also known as 3D printing. Additive manufacturing technology is highly valued for bone implant fabrication because it allows for complex and tailored geometries that reduce the elastic modulus mismatch between the implant and surrounding bone, thereby preventing bone resorption caused by stress shielding [1–4]. Additionally, AM facilitates the production of patient-specific implants, leading to improved patient outcomes [5–7]. Despite the numerous benefits of AM, including the ability to create intricate and sophisticated geometries, the mechanical performance of 3D printed metallic biomaterials, in general, and their fatigue performance, in particular, are not yet well understood. This is especially the case for architected biomaterials, known as *meta*-biomaterials. That is because both microarchitectural design parameters,

including unit cell type, unit cell dimensions, and unit cell distribution [8–10] as well as AM-related factors, such as incomplete fusion, cracks, metallic inclusions, segregation, residual stresses, and metallurgical imperfections [11–13] influence the mechanical performance of such architected biomaterials. An additional contributing factor is the anisotropy of lattice structures generated through laser powder bed fusion (L-PBF), which pertains to the microstructure and geometrical imperfections inherent in the manufactured parts [13–15]. Specifically, variations in the cross-sectional profiles, the offset of struts from their ideal axis, as well as irregularities in the elliptical cross-section of struts and their deviation from the ideal axis may play important roles in this regard [13]. These geometric deviations exert a substantial influence on the mechanical behavior of lattice structures and their effects extend beyond a mere uniform reduction in the stiffness and strength [13]. Further investigation is, therefore, necessary to optimize AM processes for the fabrication of reliable and durable bone implants for biomedical

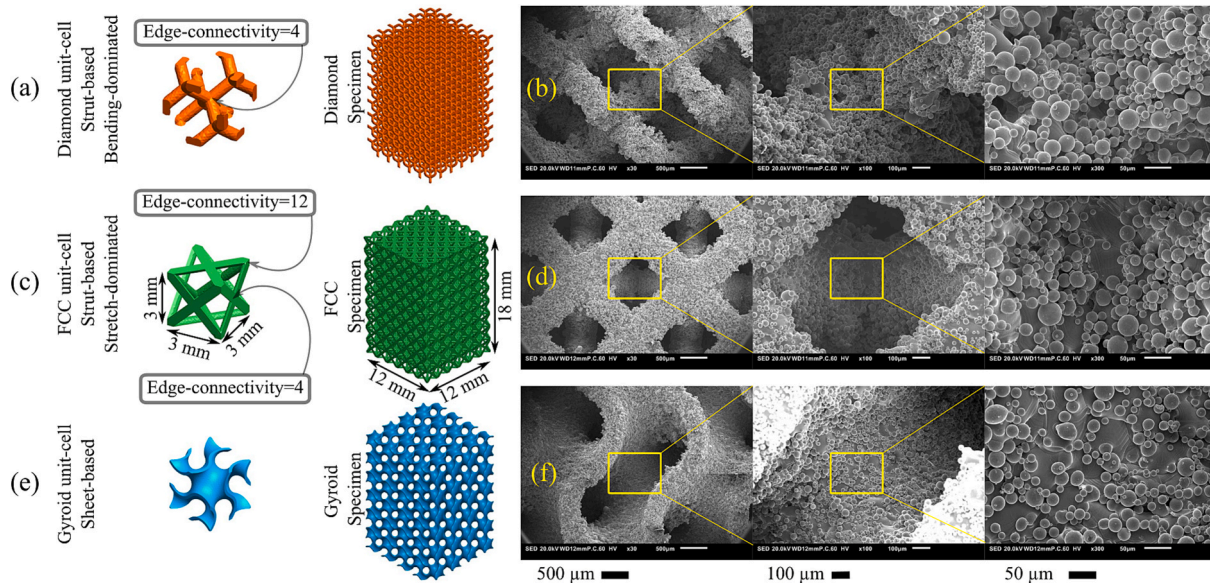**Fig. 1.** A schematic representation of the unit cells for each geometry, with dimensions of $3 \times 3 \times 3$ (mm^3), and test samples with a cross section of 12×12 (mm^2) and a height of 18 mm. $4 \times 4 \times 6$ unit cells were tessellated in 3D lattice samples. Each row contains the SEM image of a LPBed sample at the relative density of 25 %, with magnification levels of 30×, 100 × and 300 × for Diamond (a-b), FCC (c-d) and (e-f) Gyroid geometry.

applications.

The influence of material defects on the fatigue life of orthopedic implants is a subject of significant interest for researchers, as fatigue strength represents a critical attribute of these implants. In the development of orthopedic implants, such as hip joint replacements, preference has been given to forged products over cast products due to their superior fatigue strength [16,17]. In the context of 3D printed components, the impact of internal porosity and surface roughness on the fatigue strength is often more pronounced as compared to that of microstructure, as stress concentration sites are created by rough surfaces and/or pores, leading to a reduction in the fatigue life [18]. Although the individual contributions of residual stresses, grain size, and ductility to fatigue life may be limited, an extended fatigue life for fabricated parts can be achieved through a combination of enhanced ductility and reduced residual stresses particularly when accompanied with surface smoothening treatments after AM [19–22].

It is typically the increased surface roughness of 3D printed parts that makes them more vulnerable to fatigue failure [23–25], as cracks typically initiate at such stress concentration sites on the surfaces. This higher surface roughness is a consequence of the intrinsic characteristics of 3D printing processes [18,26–28]. The probability of fatigue failure is proportional to the increase in the surface-to-volume ratio, as a larger surface amplifies the frequency of defects capable of initiating cracks [27,29]. Understanding and addressing these factors is essential for optimizing the performance and longevity of 3D printed orthopedic implants.

The impact of defects on reducing the fatigue strength under specific loading conditions can be influenced by the distribution of stress within an ordered porous structure, otherwise known as lattice structures. The dominant deformation mode of a lattice structure can be either stretch-dominated or bending-dominated. For a given relative density, stretch-dominated lattice structures exhibit greater stiffness and strength than their bending-dominated counterpart [30,31]. They also show more pronounced softening behavior after reaching their initial strength [32]. In bending-dominated structures, stresses are generally higher in proximity to the strut surfaces as opposed to regions closer to their neutral axis. In fact, bending induces stress localization that reaches the material's fracture strength, resulting in the overall failure of the bending-dominated structure.[32]. It is, therefore, essential to study how the deformation modes can influence the detrimental impacts of material

defects on fatigue life. By investigating these influences, a deeper understanding of the fatigue behavior of ordered porous structures can be obtained, which can result in optimized performance of such *meta*-biomaterials.

The aim of this research is thus to examine whether single struts inside a unit cell that are primarily subjected to bending exhibit a shorter fatigue life in comparison to those subjected to stretching, and to establish their correlation with triply periodic minimal surface (TPMS) structures. Additionally, the investigation aims to analyze the influence of relative density on the fatigue life of these structures. Moreover, the effect of infilling a porous structure with polymer will be explored regarding alterations in strain field and strength of these structures.

2. Materials and methods

2.1. Specimen design and modeling

In this study, two main categories of unit cell designs were studied, namely strut- and sheet-based. The strut-based group was further subdivided into two subgroups, including Diamond (D) and face centered cubic (FCC), representing bending-dominated and stretch-dominated structures, respectively. In contrast, the sheet-based group was designed with a Gyroid geometry, forming a TPMS lattice structure. The detailed geometries of different design groups are presented in Fig. 1.

For the creation of STL files for the 3D printing process, nTop commercial software (formerly nTopology) was utilized. The specimens were right-angled cuboids with a square cross-section of 12×12 mm^2 and a height of 18 mm. The cuboid volume was tessellated by the unit-cell geometries, resulting in an equal number of unit cells (*i.e.*, $4 \times 4 \times 6$) and identical unit cell dimensions of 3x3x3 mm^3 for all the specimens. Three designed relative density levels of 15 %, 25 %, and 35 % were applied to all the geometries. Since an efficient scaffold must simultaneously exhibit suitable mechanical properties and biological response potential, the selected relative densities were chosen to fulfill this requirement. According to previous studies, an optimum porosity exceeding 50 % is recommended to achieve enhanced osseointegration [33]. Higher porosity increases the scaffold's specific surface area, enhancing cell migration, nutrient delivery, and vascularization, all of which support improved osseointegration [34]. On the other hand, since the scaffolds are metallic, porosity needs to be increased to reduce

effective stiffness and avoid stress shielding. Therefore, high porosity is desirable, but it can only be achieved within the limitations of the additive manufacturing machine. Based on all these considerations, porosities of 65 %, 75 %, and 85 % were selected, corresponding to relative densities of 35 %, 25 %, and 15 %, respectively. The relative density (*RD*) was calculated by the following formula:

$$RD = \rho^*/\rho = \frac{\frac{m^*}{V}}{\rho} = m^*/\rho.V \tag{1}$$

where ρ^* is the density of the lattice structure, ρ is the density of the solid material, m^* is the mass of the lattice structure, and V is the total volume of the specimen. Accordingly, the porosity (*P*) of the specimens was defined as: $P = 1 - RD$.

2.2. Manufacturing techniques

Using the L-PBF technique, otherwise known as selective laser melting or direct metal printing, the specimens were manufactured from Ti-6Al-4 V ELI (grade 23, Carpenter) metallic alloy powders with a particle size D_{50} of 31 μm. A DMP Prox320 (3D Systems, Leuven) machine was used for manufacturing all the specimens, and a double contour with hatching scan strategy was employed. A layer thickness of 45 μm was used, with scan parameters that resulted in a volumetric energy density of $e = 63$ J/mm^3 for the hatching. The volumetric energy was calculated as $e = p/vht$, where p is the laser power, v the scanning speed, h the is hatching distance, and t is the layer thickness. A total of 166 specimens were produced. A representative sample of each geometry type was imaged using a scanning electron microscope (SEM, JSM-IT100, JEOL, Japan).

To examine the effects of infilling a lattice structure with polymer on its deformation mode and strength, the L-PBFed samples were divided into two primary groups: "as-built" and "in-filled". For the in-filled group, ClaroCit™ resin was utilized. The resin was prepared by blending the powder and liquid components at a mass ratio of 2:1. The powder component in this blend consisted of dibenzoyl peroxide, while the liquid component contained a mixture of organic solvents, binders, and additives.

Several silicon molds were employed to infill the lattice structures. The silicone molds were cast using FFF-printed (fused filament fabrication) plastic molds, which had cross-sectional dimensions matching those of the samples and a height that was 5 mm greater than the samples. ClaroCit™ polymer was poured into the molds, and the samples were promptly inserted within molds with slight pressure. Additional polymer was then added to completely cover the samples. Finally, the silicon molds containing the samples were placed in a pressure pot and pressurized up to 2 bars for an hour to prevent bubble formation inside the samples. Once the polymer solidified, the samples were removed from the molds, and extra polymer layers on different sides of the samples were removed using 400 to 800 grit sandpaper and "Struers" polishing equipment. For each porosity in each geometry, three samples were infilled with polymer. To calculate the percentage of infiltrated space in the in-filled samples, the density of the cured resin was needed to be determined. To obtain this, cubic samples were prepared from the cured resin. The density was then calculated by dividing each sample's mass by its volume.

2.3. Quasi-static mechanical testing

To obtain the mechanical properties, quasi-static compression tests were conducted according to the ISO standard for the mechanical testing of porous metallic materials (*i.e.*, ISO13314:2011) using a tensile test machine (Zwick 100, Germany, load cell = 100 kN) under displacement control. The crosshead displacement rate was set to 0.018 mm/s, corresponding to a strain rate of 0.001 s^{-1}, while force, displacement, and time were recorded at a sampling frequency of 70 Hz. The same standard

was employed to calculate the mechanical properties of the lattice structures. The terminology established by this standard has been consistently applied throughout all figures and text in the present paper, denoted as follows: Stress (σ), strain (ϵ) which were obtained respectively by dividing the applied force by the cross-sectional area (=144 mm^2) and the crosshead displacement by the initial height of the sample (=18 mm).

Quasi-elastic gradient (or elastic modulus, *E*) was defined from the maximum slope of the linear region of the stress–strain curve for each sample. The initial maximum compressive strength (σ_{max}) was defined as the maximum stress observed. Compressive offset stress (σ_{yield}) for each sample was determined by the stress at 2 % strain, and the corresponding strain was considered as the compressive yield strain (ϵ_{yield}). The area under the stress–strain curve, ranging from zero to the initial maximum compressive strength, was regarded as an index of energy absorption per unit volume (*W*).

2.4. Compression-compression fatigue mechanical testing

To conduct high-cycle fatigue tests, two testing facilities were utilized (Instron E10000, UK, load cell = 10 kN and MTS 500kN, USA, load cell = 50 kN), taking into account the capacities of the available mechanical testing machines and the need for minimizing fatigue testing run time.

The fatigue load regimes for all the samples were characterized by a compression-compression load at a speed of 0.02 mm/s. The maximum cyclic compressive forces for each sample were then calculated proportionally to their calculated σ_{yield} (Table 2). For each sample, a set of four maximum cyclic compressive loads ($\sigma_{C(max)}$) of $0.2 \times \sigma_{yield}$, $0.4 \times \sigma_{yield}$, $0.6 \times \sigma_{yield}$, and $0.8 \times \sigma_{yield}$ were defined. The $\sigma_{C(max)}$ *vs.* the number of fatigue cycles, *N*, plots were shown on a log–log scale calculated from Python's "curve_fit" module from the "scipy.optimize" library.

The compression-compression fatigue force ratio was set at 10, thereby, setting the minimum compressive force for each fatigue loading regime at 0.1 times the maximum compressive force (see Table 2). All fatigue tests were conducted using a sinusoidal load with a frequency of 15 Hz. The stress-control mode of the testing machine was utilized for conducting all fatigue tests, and the point at which the displacement value exceeded 0.5 mm, corresponding to 2.7 % strain over one cycle, was considered as the test endpoint. This termination criterion was defined to ensure that all the samples would fail, while preventing any damage to the testing machine.

2.5. DIC measurements

In order to gain insights into the full-field strain distributions in different *meta*-biomaterial groups and their failure mechanisms during uniaxial quasi-static compressive mechanical testing, digital image correlation (DIC) was performed on samples with 25 % relative density. Full-field strain maps were obtained (the equivalent von Mises strains at $0.8 \times \sigma_{yield}$) at a frequency of 1 Hz using a 3D DIC system (Q-400, two cameras each with 12 MPixel, LIMESS GmbH, Krefeld, Germany) and its associated software (Instra 4D v4.6, Danted Dynamics A/S, Skovunde, Denmark).

2.6. Statistical analysis

A one-way ANOVA was performed using python's "SciPy" library to compare the properties of the as-built and in-filled groups, specifically *E*, σ_{yield}, ϵ_{yield}, *W*, across three relative densities (*i.e.*, 15 %, 25 %, and 35 %). Subsequently, Tukey's Honestly Significant Difference (HSD) post-hoc test was conducted using the "statsmodels" library of python. The results of Tukey's post-hoc test are presented in Table 4.

Table 1

The relative density of the CAD models and as-built 3D printed specimens as well as the infiltrated space within the in-filled samples. The relative density of the CAD models was calculated using CAD software (nTopology™, USA). In order to achieve intended relative densities, the thickness of each design geometry was adjusted.

Lattice groups	Relative density of the CAD models [%]	Relative density of the as-built samples [%]	Infiltrated space within the in-filled samples [%]
D-15	14.43	25.75 ± 0.77	88.12 ± 0.55
D-25	24.46	35.29 ± 0.73	89.37 ± 6.77
D-35	35.48	45.82 ± 1.69	89.35 ± 7.42
F-15	14.83	27.33 ± 0.78	88.69 ± 8.58
F-25	24.67	35.29 ± 0.73	88.9 ± 2.14
F-35	35.42	48.40 ± 1.10	96.17 ± 2.14
G-15	15.05	26.61 ± 1.66	88.81 ± 0.62
G-25	25.07	36.12 ± 0.06	90.24 ± 3.07
G-35	35.05	45.07 ± 1.32	91.89 ± 3.11

Table 2

The maximum fatigue load for lattice structure in different groups across different relative densities.

Geometry	Group name	F_{yield} [kN]	$F_{Cyclic(max)} =$			
			$0.8 \times F_{yield}$ [kN]	$0.6 \times F_{yield}$ [kN]	$0.4 \times F_{yield}$ [kN]	$0.2 \times F_{yield}$ [kN]
Diamond	D-15	9.45	7.56	5.67	3.78	1.89
	D-25	19.19	15.35	11.51	7.68	3.84
	D-35	32.23	25.78	19.34	12.90	6.45
FCC	F-15	13.70	10.96	8.22	5.48	2.74
	F-25	24.51	19.61	14.71	9.80	4.90
	F-35	40.03	32.02	24.02	16.01	8.01
Gyroid	G-15	16.35	13.08	9.81	6.54	3.27
	G-25	25.95	20.76	15.57	10.38	5.19
	G-35	38.78	31.02	23.27	15.51	7.76

3. Results and discussion

SEM images of the 3D printed samples from different groups (Fig. 1b, d, and f) showed a significant presence of partially unmolten titanium alloy powder particles adhered to the surfaces, resulting in rough surfaces prone to crack initiation. Notably, the accumulation of particles on the surface of Gyroid samples was comparatively lower than on other structures. It is, however, important to mention that no statistical analysis of surface roughness was performed, thus limiting the assessment to qualitative observations.

Given the considerable surface roughness observed across all the samples, it was expected that the fatigue life of them would be lower than the identical structures with smoother surface conditions.

Furthermore, it was observed that all L-PBFed samples exhibited a relative density approximately 10 % higher than the nominal relative density of their CAD models, attributed to the additional unmolten powder particles present within the lattice structures. Despite this discrepancy, the deviation in relative density across all groups remained below 4 % (Table 1). This difference was substantially smaller than the relative density variation observed between the three levels of porosity within a single geometry (≈10 %), enabling a comparative analysis of their mechanical and fatigue properties.

The last column of Table 1 lists the percentage of infiltrated space within the in-filled samples. To calculate these values, determining the density of the cured resin was needed. This density was found to be approximately 0.00134 g/mm³. The reported data indicate incomplete filling by resin across all the in-filled samples. The presence of unmolten powder particles, as mentioned earlier, may have impeded full resin penetration into the structures. Table 3 summarizes the mechanical properties (*i.e.*, E, σ_{max}, σ_{yield}, ϵ_{yield}, W) for both as-built and in-filled samples. The quasi-static compression stress–strain results for all as-built samples are presented in Fig. 2a. The stress–strain curves for the three different geometries exhibited similar trends, consisting of a linear elastic region followed by yielding and reaching to a maximum compressive strength. The samples with Gyroid geometry had more extended smooth plateau regions after their maximum compressive stress. Furthermore, they were capable of maintaining functionality beyond the point of maximum compression stress without rupture. As it is illustrated in Fig. 2a, the curves after maximum point remain smooth into some extent. Samples of Diamond and FCC geometries experienced a sudden drop in their stress–strain curves, specifically after the maximum stress. Among the different sample geometries and different relative density levels, only D-35 samples exhibited catastrophic failure, demonstrating a brittle-like fracture (Fig. 2a). This could be due to the fact the simultaneous breaking of some struts within those structures, leading to overall failure. The causes for this observation remain unclear to the authors and should be investigated in further studies. As expected, the elastic modulus of all the samples increased with relative density (Fig. 2b). At identical relative densities, the samples with Gyroid geometry exhibited the highest elastic moduli, while those with Diamond geometry had the lowest which is in agreement with the results of previous studies [35,36]. The largest difference in the elastic moduli of the different groups was observed at the lowest relative density, where Gyroid has the highest and Diamond had the lowest modulus (Fig. 2b). This difference diminished as the relative density increased, since the properties of the lattice structure began to more closely resemble those of the base titanium alloy.

The yield strength (σ_{yield}), yield strain (ϵ_{yield}), and the maximum compressive strength (σ_{max}), were also increased with relative density (Fig. 2c, d and e). At identical relative density levels, samples with Gyroid geometry showed the highest yield and maximum compression
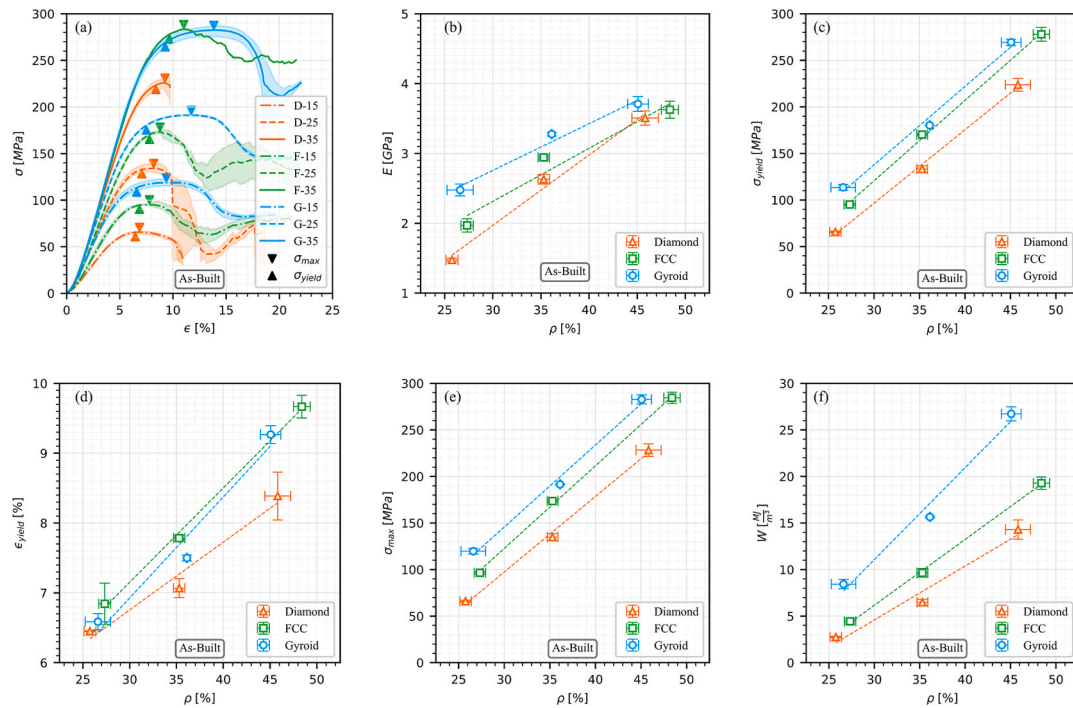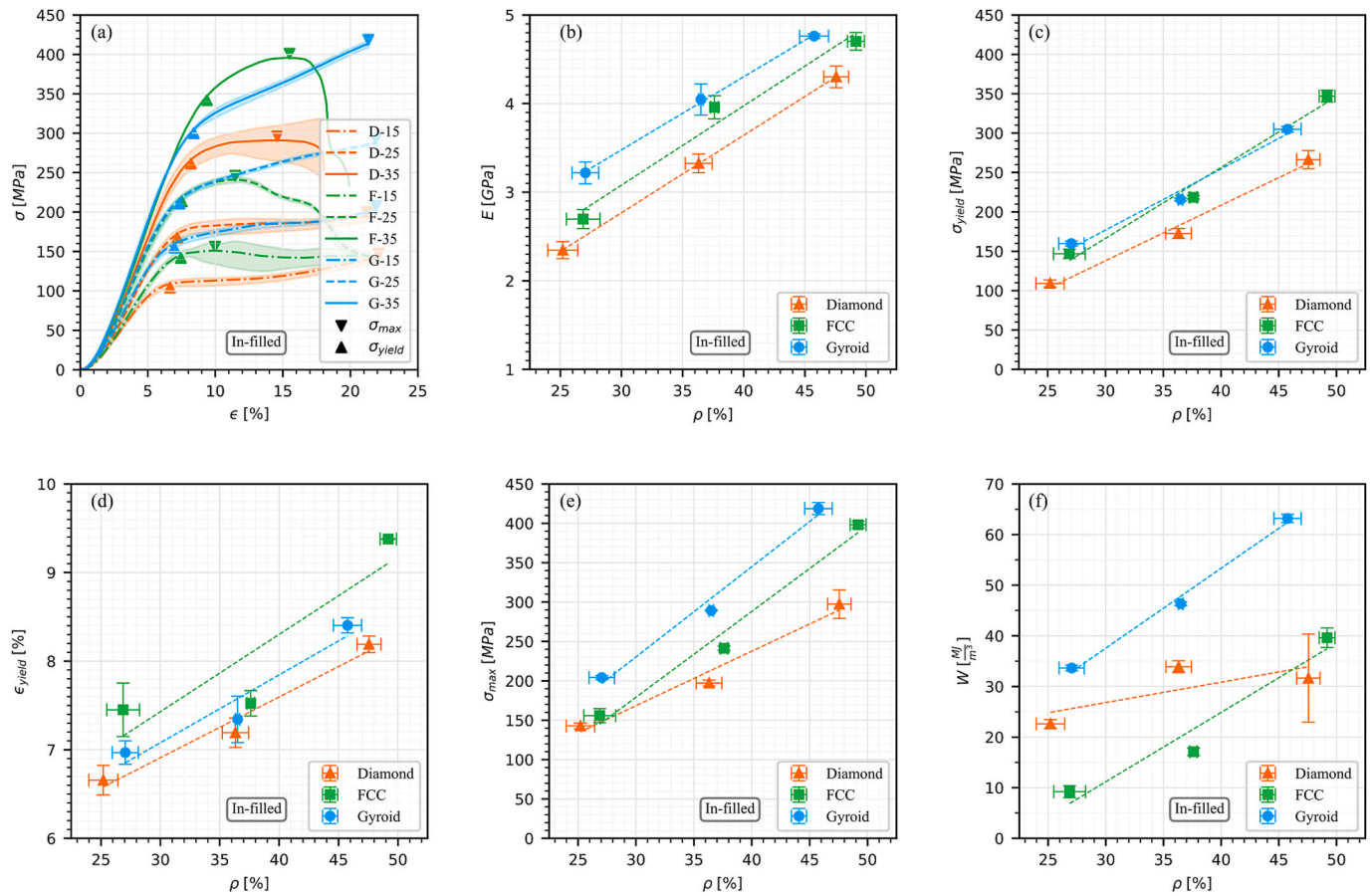
Table 3

Summary of mechanical properties quasi-elastic gradient (E), maximum compressive strength (σ_{max}), compressive Offset Stress at 2% Plastic Strain (σ_{yield}), The Overall Strain at Compressive Offset Stress (ϵ_{yield}), and Energy Absorption Per Unit Volume (W) for both as-built and in-filled samples.

	Property	D-15	D-25	D-35	F-15	F-25	F-35	G-15	G-25	G-35
As-built	$E[GPa]$	1.474 ± 0.024	2.630 ± 0.070	3.507 ± 0.101	1.969 ± 0.094	2.942 ± 0.033	3.626 ± 0.122	2.477 ± 0.086	3.277 ± 0.027	3.709 ± 0.106
	$\sigma_{yield}[MPa]$	65.64 ± 1.09	133.2 ± 3.6	223.8 ± 6.9	95.15 ± 1.27	170.2 ± 0.9	278.0 ± 7.3	113.5 ± 3.1	180.2 ± 0.1	269.3 ± 3.4
	$\epsilon_{yield}[\%]$	6.45 ± 0.01	7.07 ± 0.13	8.39 ± 0.34	6.85 ± 0.30	6.85 ± 0.3	9.67 ± 0.16	6.59 ± 0.11	7.5 ± 0.04	9.27 ± 0.13
	$\sigma_{max}[MPa]$	65.90 ± 1.16	134.8 ± 3.8	228.4 ± 6.743	96.53 ± 1.43	173.6 ± 1.5	284.5 ± 6.0	119.7 ± 3.0	191.5 ± 0.2	282.7 ± 4.9
	$W[MJ/m^3]$	2.752 ± 0.077	6.480 ± 0.322	14.30 ± 1.03	4.440 ± 0.279	9.651 ± 0.463	19.28 ± 0.67	8.433 ± 0.503	15.65 ± 0.10	26.72 ± 0.76
In-filled	$E[GPa]$	2.346 ± 0.096	3.324 ± 0.106	4.302 ± 0.123	2.696 ± 0.107	3.958 ± 0.130	4.702 ± 0.100	3.218 ± 0.123	4.046 ± 0.175	4.762 ± 0.025
	$\sigma_{yield}[MPa]$	109.2 ± 4.5	172.6 ± 6.3	266.4 ± 11.5	146.8 ± 5.8	218.35 ± 2.1	346.9 ± 7.6	159.7 ± 3.3	215.7 ± 1.9	304.9 ± 3.5
	$\epsilon_{yield}[\%]$	6.66 ± 0.17	7.19 ± 0.17	8.19 ± 0.09	7.45 ± 0.3	7.52 ± 0.14	9.38 ± 0.01	7.34 ± 0.26	8.4 ± 0.09	
	$\sigma_{max}[MPa]$	142.8 ± 3.7	197.2 ± 3.7	297.4 ± 18.0	155.8 ± 8.9	241.3 ± 2.9	398.2 ± 4.4	204.2 ± 2.6	289.3 ± 0.7	418.7 ± 7.7
	$W[MJ/m^3]$	22.61 ± 0.84	33.9 ± 1.18	31.64 ± 8.70	9.22 ± 1.18	17.11 ± 0.73	39.62 ± 1.93	33.64 ± 0.56	46.33 ± 0.36	63.19 ± 0.82

Fig. 2. The results of the quasi-static compression test conducted on as-built samples. a) The stress *vs.* strain-strain curves for different geometries identified by colors and relative densities by line patterns (a). The change of mechanical properties E (b), yield stress (σ_{yield}) (c), yield strain (σ_{yield}) (d), maximum compressive strength (σ_{max}) (e), and energy absorption per unit volume (W) (f) *vs.* true relative densities are also shown.

Fig. 3. The results of the quasi-static compression test conducted on in-filled samples. The stress *vs.* strain curves for different geometries identified by colors and relative densities by line patterns (a). The change of mechanical properties E (b), yield stress (σ_{yield}) (c), yield strain (ϵ_{yield}) (d), maximum compressive strength (σ_{max}) (e), and energy absorption per unit volume (W) (f) *vs.* true relative densities are also shown.

stress, while those with Diamond geometry showed the lowest. The F-35 samples had slightly higher yield stress, as compared to the G-35 samples, which can be attributed to the slightly higher relative densities of these structures during the manufacturing processes. It can be argued that bending-dominated structures have lower yield and maximum compressive strength since each strut is subjected to bending loads. In such case, the central part of the struts does not reach their full load-bearing capacity, while the surfaces of them, start experiencing failure due to bending stress (imagine a beam where the central area is less loaded, but the outer areas, especially the outer layer, are highly stressed). Stretch-dominated structures, on the other hand, have struts with minimal cross-section areas under bending load. As the struts mainly tolerate stretch loads, this allows the structure to utilize more of its load-bearing capacity effectively. This results in enhanced yield and maximum compressive strength, compared to their bending-dominated counterparts. The sheet-based Gyroid structures, have the highest yield and maximum compressive strength compared to the other topologies. This is due to the fact that they have smooth surface with minimal mean curvature and therefore less prone to stress concentration. On the other hand, strut-based structures, which are more prone to stress concentration at edge connections, exhibit lower yield and maximum compressive strength Among these, bending-dominated Diamond structures have the lowest values (Fig. 2c, d, and e).

The samples with Gyroid geometry had a wider post-yield curve with a more extended plateau region after their maximum compressive stress (σ_{max}), indicating these structures can absorb more energy as compared with other geometries (Fig. 2a). The obtained energy absorption per unit volume (W) for the Gyroid structures exhibits the highest values, whereas the Diamond structures show the lowest (Fig. 2f).

The yield strain (ϵ_{yield}) increased with the relative density of the samples (Fig. 2d). The yield strains of Gyroid and FCC samples were similar, particularly at the lower relative density value of 15 % (Fig. 2d). At the lowest relative density, samples with different geometries exhibited approximately equal yield strains, regardless of the geometry of their unit cells. As the relative density increased, the difference in yield strain between the Diamond samples and the other two groups became more pronounced. While yield strain values tend to converge to the same value as the relative density decreases, E approaches a constant value as the relative density increases. It can be stated that the fracture mechanism of these structures remains distinct even as they approach a fully solid state. The failure mode of Gyroid samples displayed distinct characteristics as compared with other geometries. This distinction arises from the geometric properties of TPMS, which as mathematical surfaces, are characterized by differentiability, smoothness, and minimal mean curvature. These properties facilitate the uniform distribution and smooth transition of stress throughout the structure since minimal surfaces balance the principal curvatures, removing stress concentrations at sharp angles and evenly distributing mechanical loads [37,38]. It is important to note that, theoretically, a TPMS with zero mean curvature ideally exist in zero wall thickness. Consequently, any increase in the thickness of TPMS walls represents a deviation from this ideal mathematical model [39]. In practice, realizing a TPMS configuration requires assigning a finite wall thickness. However, increasing the wall thickness leads to greater deviation from zero mean curvature, moving the structure further away from the TPMS's theoretical optimal characteristics, causing increased stress concentrations at higher relative densities. In contrast, structures with thinner TPMS walls, are less susceptible to stress concentration, resulting in superior mechanical properties.

When comparing the in-filled samples, which imitate lattice structures resembling bone-ingrowth in the scaffold, a distinct stress–strain behavior was observed in comparison with the as-built samples. Particularly, the in-filled Gyroid samples showed work-hardening behavior after yield (Fig. 3a). For both the stretch-dominated and bending-dominated structures, the post-yield behavior were extended, likely due to the interaction between the filler and the microstructures of

Table 4

The Results of Tukey's HSD post-hoc test, comparing different mechanical properties of as-built and in-filled groups across three relative densities (15%, 25%, and 35%). For details on significance indicators, see the table footnote.

| Group (1)	Group 2	p-value				
		E	σ_{yied}	ϵ_{yield}	σ_{max}	W
D-15 (As-built)	D-15 (In-filled)	**	**	NS	**	**
D-15 (As-built)	F-15 (As-built)	*	**	NS	NS	*
D-15 (As-built)	F-15 (In-filled)	**	**	**	NS	**
D-15 (As-built)	G-15 (As-built)	**	**	NS	NS	**
D-15 (As-built)	G-15 (In-filled)	**	**	NS	**	**
D-15 (In-filled)	F-15 (As-built)	*	NS	NS	**	*
D-15 (In-filled)	F-15 (In-filled)	NS	**	*	**	NS
D-15 (In-filled)	G-15 (As-built)	NS	NS	NS	**	NS
D-15 (In-filled)	G-15 (In-filled)	**	**	NS	*	**
F-15 (As-built)	F-15 (In-filled)	**	**	NS	NS	**
F-15 (As-built)	G-15 (In-filled)	*	NS	NS	NS	*
F-15 (As-built)	G-15 (In-filled)	**	**	NS	**	**
F-15 (In-filled)	G-15 (As-built)	NS	**	*	NS	NS
F-15 (In-filled)	G-15 (In-filled)	**	NS	NS	**	**
G-15 (As-built)	G-15 (In-filled)	**	**	NS	**	**
D-25 (As-built)	D-25 (In-filled)	**	**	NS	**	**
D-25 (As-built)	F-25 (As-built)	NS	**	*	NS	NS
D-25 (As-built)	F-25 (In-filled)	**	**	NS	*	**
D-25 (As-built)	G-25 (As-built)	**	**	NS	*	**
D-25 (As-built)	G-25 (In-filled)	**	**	NS	**	**
D-25 (In-filled)	F-25 (As-built)	*	NS	NS	**	*
D-25 (In-filled)	F-25 (In-filled)	**	**	NS	**	**
D-25 (In-filled)	G-25 (As-built)	NS	NS	NS	**	NS
D-25 (In-filled)	G-25 (In-filled)	**	**	NS	**	**
F-25 (As-built)	F-25 (In-filled)	**	**	NS	NS	**
F-25 (As-built)	G-25 (As-built)	NS	NS	NS	NS	NS
F-25 (As-built)	G-25 (In-filled)	**	**	NS	**	**
F-25 (In-filled)	G-25 (In-filled)	**	**	NS	NS	**
F-25 (In-filled)	G-25 (In-filled)	NS	NS	NS	**	NS
G-25 (As-built)	G-25 (In-filled)	**	**	NS	**	**
D-35 (As-built)	D-35 (In-filled)	**	**	NS	**	**
D-35 (As-built)	F-35 (As-built)	NS	**	**	NS	NS
D-35 (As-built)	F-35 (In-filled)	**	**	**	**	**
D-35 (As-built)	G-35 (As-built)	NS	**	*	**	NS
D-35 (As-built)	G-35 (In-filled)	**	**	NS	**	**
D-35 (In-filled)	F-35 (As-built)	**	NS	**	**	**
D-35 (In-filled)	F-35 (In-filled)	*	**	**	NS	*
D-35 (In-filled)	G-35 (As-built)	**	NS	**	NS	**
D-35 (In-filled)	G-35 (In-filled)	*	**	NS	**	*
F-35 (As-built)	F-35 (In-filled)	**	**	NS	**	**
F-35 (As-built)	G-35 (As-built)	NS	NS	NS	NS	NS
F-35 (As-built)	G-35 (In-filled)	**	**	**	**	**
F-35 (In-filled)	G-35 (As-built)	**	**	NS	**	**
F-35 (In-filled)	G-35 (In-filled)	NS	**	**	**	NS
G-35 (As-built)	G-35 (In-filled)	**	**	*	**	**

**$p < 0.001$.
*$p < 0.05$.
NS: $p \geq 0.05$ (Not Significant).

those lattice structures. The filler polymer ($E = 0.68 \pm 0.13$ GPa) contributed to load bearing capacity by supporting the struts or walls to prolong the plastic deformation region until the struts or walls reached their full load-bearing capacity. All other mechanical properties increased accordingly in comparison with those of the as-built samples (Fig. 3b-f). Moreover, the yield strain of the FCC samples is higher than that of the Gyroid samples; however, this difference is not significant for the as-built samples (Table 4).

The in-filled samples did not show catastrophic failure (Fig. 4). In the FCC and Diamond groups, at higher relative densities, 45° macro cracks were observed in the structure beyond their maximum stress points (Fig. 4-right), indicating a dominant shear failure mechanism in these structures. Conversely, the Gyroid samples primarily underwent severe compression without macroscopic cracks. At the lowest relative density, lateral barreling emerged as the principal deformation mode under loading beyond the yield point.

Comparing as-built and in-filled samples at identical relative densities, statistically significant differences (p < 0.05) were observed in all
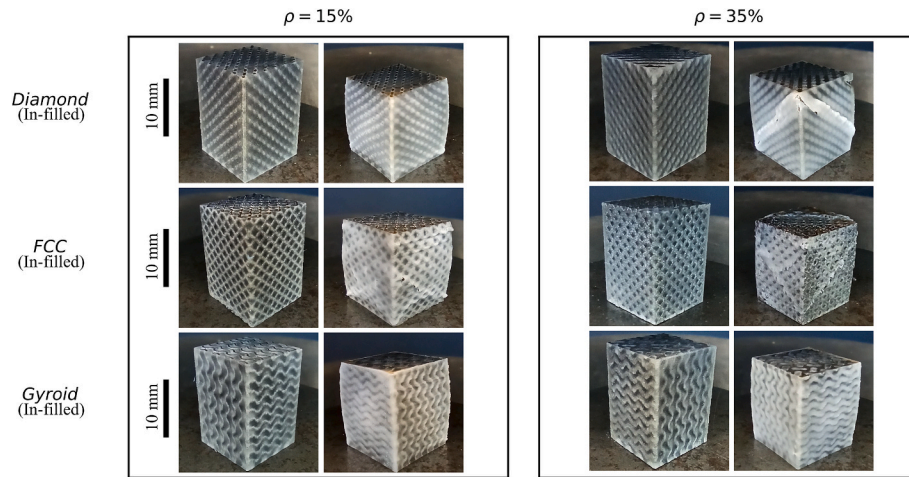
Fig. 4. The in-filled samples before and after testing, illustrating catastrophic failure in F-35 and D-35. This failure occurred along the shear plane at a 45° angle relative to the compressive load direction for both designs.
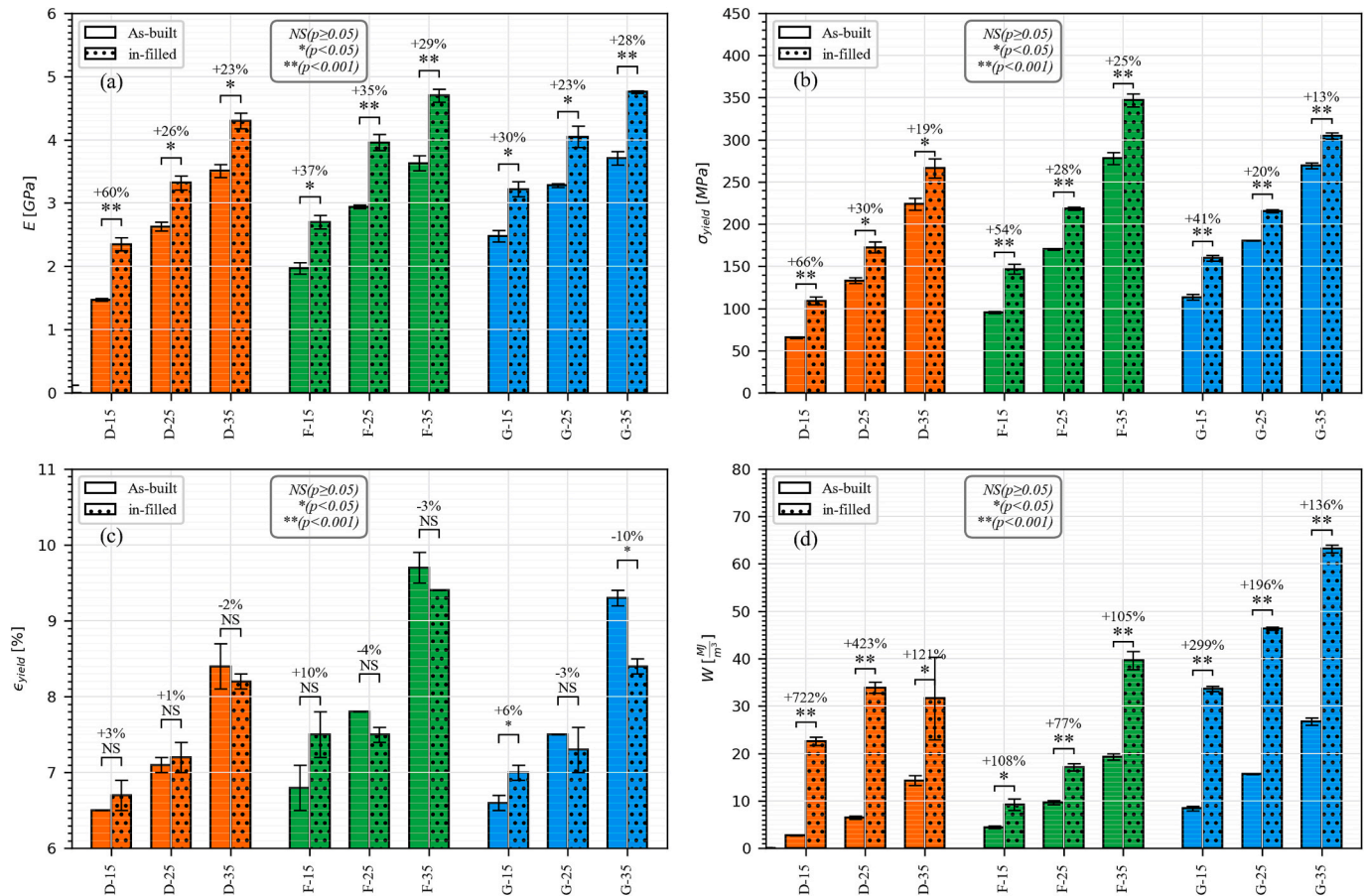
Fig. 5. A comparative analysis of mechanical properties between as-built and in-filled samples presented in a bar chart. Different geometries are color-coded, and in-filled samples are distinguished by a dotted pattern. The change of mechanical properties E (a), yield stress (σ_{yield}) (b), yield strain (ϵ_{yield}) (c), and energy absorption per unit volume (W) (d) are also shown.

mechanical properties except compressive yield strain (Fig. 5). The elastic moduli, yield stress, and energy absorption of the in-filled samples were in average 32 %, 32.8 %, and 243 % higher than those of the as-built samples, respectively (Fig. 5a, b, and d).

These findings provide remarkable insight in the design of bone scaffolds. Specifically, bone scaffolds must be harmonized with the displacement field, guiding the surrounding bone in a way that prevents stress shielding. They must also possess the ability to withstand impact loads, meeting the regular expectations for bony tissue functionality, and exhibit a longer life cycle to decrease the need for revisional surgeries due to scaffold failure.

The comparison of equivalent von Mises true strain distributions at 80 % of the yield stress across three different geometries revealed insights into their respective failure mechanisms (Fig. 6a-c). As-built
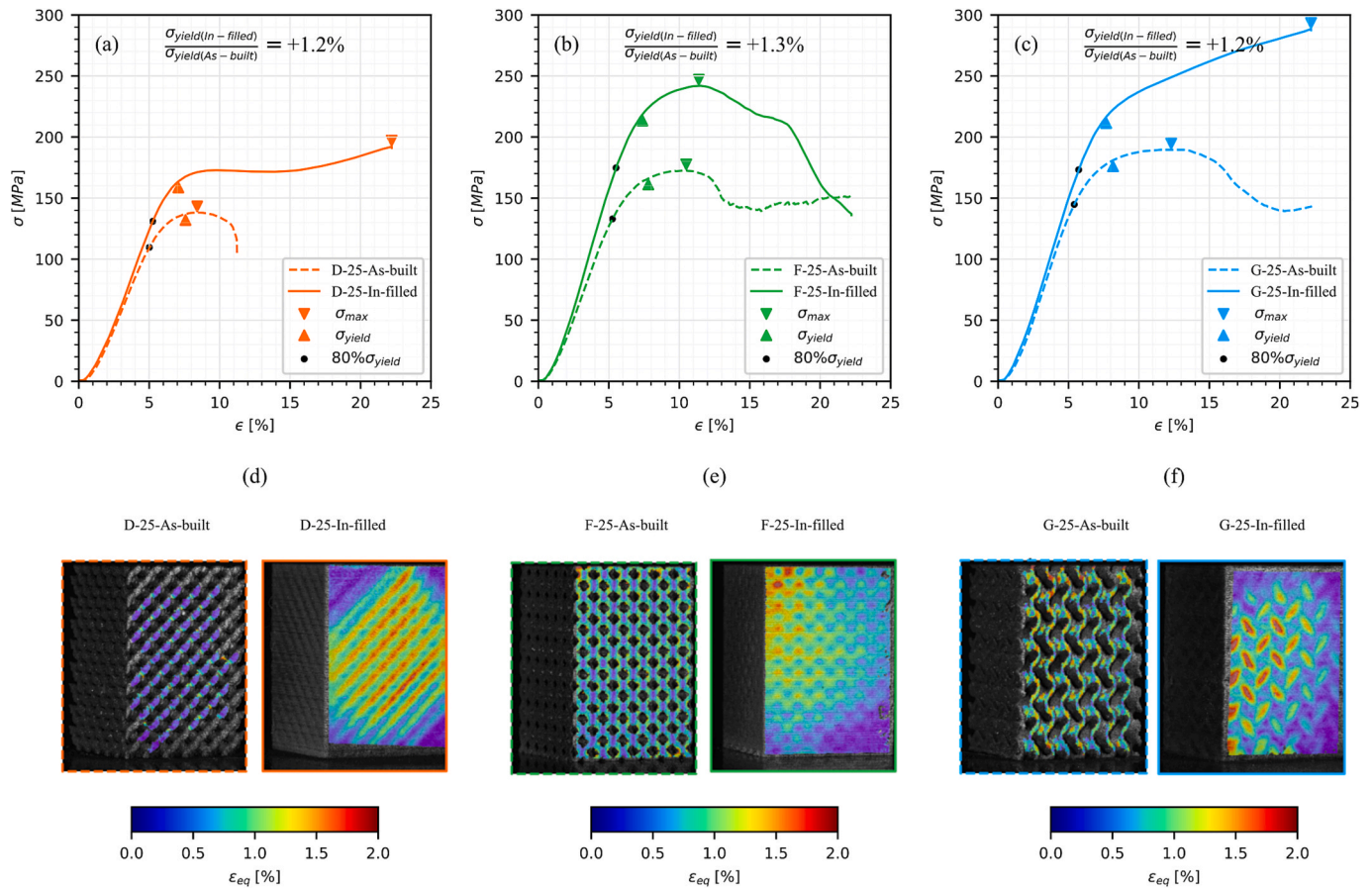
Fig. 6. The results of equivalent von Mises strain field distribution obtained by DIC technique for the 25 % relative density groups of as built and in-filled samples. a-c) The stress–strain curves of the DIC samples indicating different mechanical properties (*i.e.*, σ_{max}, σ_{yield} and $0.80 \times \sigma_{yield}$ corresponding to the points where the subfigures d to f were captured). d-f) The DIC images of the samples showing the equivalent von Mises distribution when the stress reached 80 % of the sample's yield stress.

Diamond lattice configurations demonstrated significant strain concentrations at the connections of struts (Fig. 6d), leading to premature failure under lower stress levels. Similarly, in the case of FCC structure, although to a lesser extent, the highest strains were observed in areas where struts were not aligned with the direction of applied load (Fig. 6e). Upon filling the lattice structures, a shift in the deformation pattern emerged, with strain concentrations primarily observed within the polymer sections rather than the metallic sections (Fig. 6d-f). This shift was expected due to the polymer's lower elastic modulus relative to the metal used. Interestingly, the polymer's lower modulus presented a beneficial aspect to the lattice structures by enabling the initial high-deformation regions to be supported more effectively. This support facilitated stress transmission to the adjacent polymer areas, thus enhancing the structural integrity. Ultimately, the experimental findings shed light on the stress distribution mechanisms within polymer-infilled metallic structures, revealing that these in-filled structures possess approximately + 1.2 times the strength of as-built lattices (Fig. 6a-c).

The analysis of compressive stress versus the number of cycles to failure across three geometries showed a consistent trend (Fig. 7). Notably, the sheet-based lattice structures exhibited superior fatigue strength, withstanding over one million cycles at stress levels < 0.3 × σ_{yield} (Fig. 7c), in comparison with the structures governed by bending or stretching mechanisms. As it was expected, an increase in the relative density leads to an extended number of cycles to failure and higher fatigue strength (Fig. 7a-c). As previously discussed, the mechanical properties, particularly yield strength and maximum compressive stress of the in-filled structures had been significantly enhanced, therefore, it can be reasonably argued that the in-filled

structures are likely to demonstrate an extended fatigue life. However, due to the time-intensive nature of fatigue tests, these experiments may be conducted in future studies.

The FCC lattice, as a stretch-dominated structure, exhibited a higher fatigue life as compared to the Diamond lattice, which is a bending-dominated structure. However, their overall fatigue life behavior remains almost similar with the increase in relative density. Fatigue life of Gyroid as an TPMS topology is much higher than strut-based structures. Additionally, fatigue life-to-stiffness ratio of Gyroid structure is slightly increases when the relative density decreases. In contrast, this ratio in Diamond and FCC decreases by decreasing relative density. It is evident that the Gyroid lattice maintains its fatigue strength even at lower relative densities. Therefore, it can be utilized in the design of structures that require lower values of relative density (lighter weight and lower stiffness) but higher fatigue strength. Upon normalizing the maximum compressive fatigue load by the yield load of each lattice type, the data converged to one master curve (Fig. 7d-f), indicating that the fatigue response depends only on their corresponding compressive yield stresses, independent of the relative density of the lattice structures. This finding provides a practical tool and guideline for the design of *meta*-biomaterials so that the fatigue life of such materials can be obtained simply by performing quasi-static tests, thereby avoiding long, extensive and costly series of fatigue tests. In this regard, one can use $\frac{\sigma_C}{\sigma_{yield}} = A \times N^B$ to predict the fatigue life of different lattice structures, where the coefficients A and B are specific to each geometry type (Fig. 7d-f). The results align with those of other studies [40,41] that investigated the fatigue lives of other unit cell types and concluded that the same normalization approach holds for these lattice structures, independent
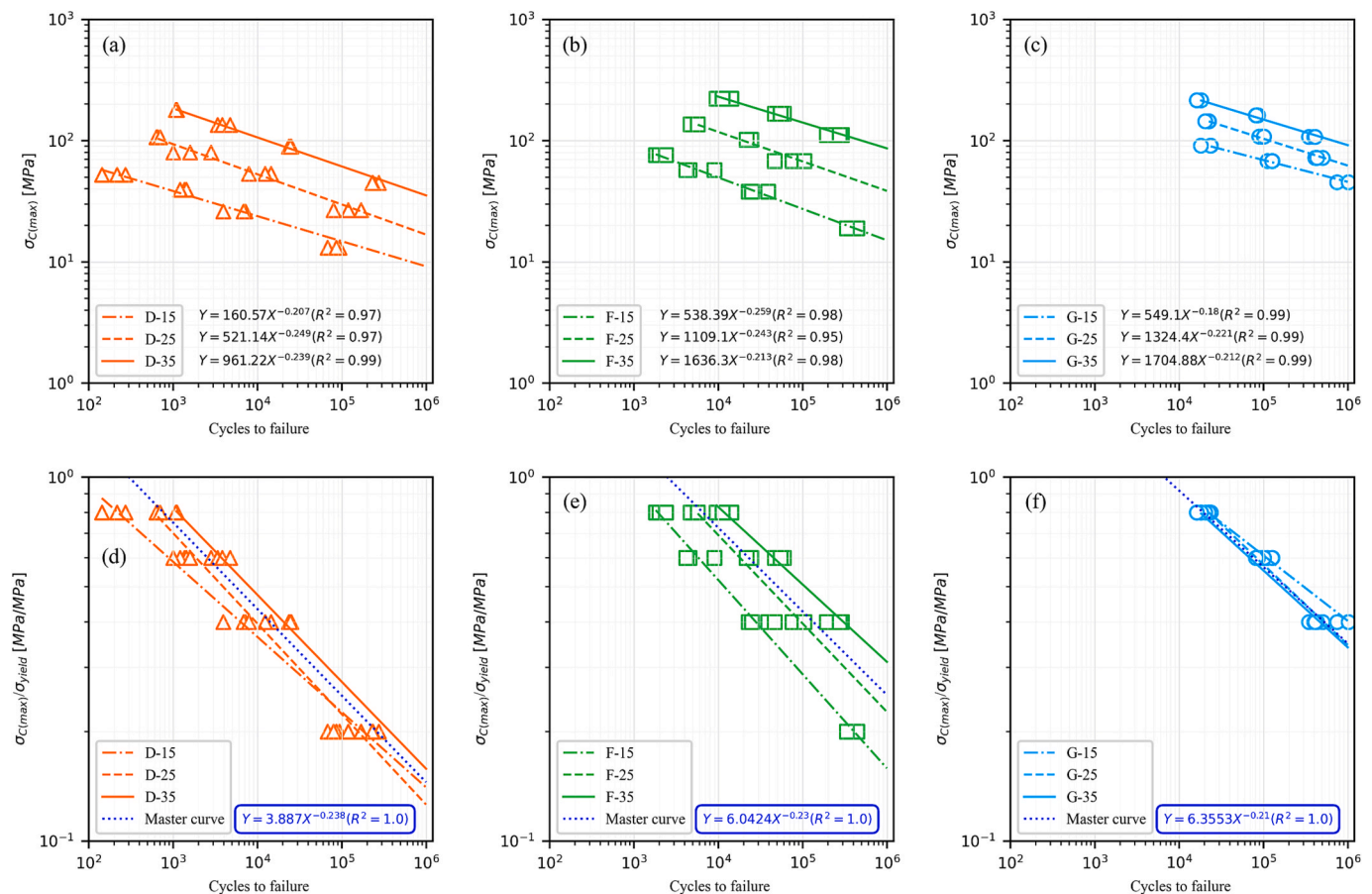
Fig. 7. The S-N curves from fatigue tests for as-built samples. Subfigures 7a to 7c illustrate the maximum cyclic stress *vs.* number of cycles to failure, while subfigures 7d to 7f present the normalized curves of the samples with respect to their yield stress. In subfigures 7a to 7c, different lines are plotted to only guide the eye while the different line patterns in sub-Fig. 7d-f are the fitted power-law curve for distinct lattice structure.

of their mechanistic feature and whether they are bending-dominated, stretch-dominated or sheet-based.

It should be noted that these results are only valid for the lattice structures under compression-compression fatigue loading, thus changing the loading conditions (*e.g.*, tension–tension fatigue loading) may alter the fatigue response of these lattice structures.

4. Conclusions

This study develops, new criteria for micro-architecture design of additively manufactured biomaterials. Three different scaffold architecture, bending-dominated, stretch-dominated and sheet-based structures in two different configurations of in-filled and as-built have been designed and fabricated using Ti-6Al-4 V biomaterial grade. An in-filled sample can imitate a scaffold with bone-ingrowth. Mechanical properties of all the samples, including elastic modulus, yield stress and strain, maximum compressive strength, energy absorption per unit volume and fatigue strength were measured and analyzed. The major findings are:

Bending-dominated structures, have the lowest mechanical strengths and the shortest fatigue life because of stress concentration and localized strain in the cross-section of the struts. Stretch-dominated structures feature struts with small cross-sectional areas under bending. Since, these struts mainly carry stretch loads, the structure more efficiently exploits its load-bearing capacity, leading to enhanced yield strength, compressive strength, and fatigue life compared with bending-dominated structures. The sheet-based Gyroid structures exhibit the highest yield, maximum compressive strength, and fatigue life among the topologies studied. This is attributed to their smooth walls with minimal mean curvature, which reduce stress concentrations and

promote a more uniform distribution of mechanical loads across the material domain.

The second design principle pertains to the different structures and their responses to relative density changes. As the relative density increases, the fatigue life of the strut-based structures is increased. However, the fatigue life of the Gyroid structures either slightly increases or remains nearly unchanged, but it does not decrease obviously, indicating a superior fatigue life-to-stiffness ratio. This means that lower stiffness can be achieved without compromising fatigue strength, which is precisely the goal in the design of orthopedic implants.

The third finding of this research, associates with the impact of polymer infiltration on structural performance. Infiltration of porous structures with polymer significantly increases the mechanical strength of the filled structure, despite only a slight increase in its stiffness. Therefore, within the process of scaffold stiffness engineering, once the desired stiffness distribution has been predicted, it can be slightly reduced to account for polymer infiltration, to ultimately achieve the desired stiffness. Additionally, this approach leads to a considerable enhancement in mechanical strength and, consequently, fatigue life. Moreover, this leads to a structure that requires less base material but demonstrates significantly enhanced strength.

These novel and significant findings, demonstrate that by strategically manipulating porosity and incorporating polymer infiltration, it is possible to design and fabricate structures that are both lighter and stronger. These design disciplines, can open up new avenues for the design and fabrication of *meta*-biomaterials with tailored mechanical properties.

CRediT authorship contribution statement

S.Kazemivand Niar: Writing – original draft, Visualization, Validation, Software, Methodology, Investigation, Formal analysis, Data curation, Conceptualization. **G. Nikaein:** Writing – review & editing, Visualization, Validation, Software, Methodology, Investigation, Formal analysis. **M.H. Sadeghi:** Writing – review & editing, Validation, Supervision, Resources, Project administration, Methodology, Investigation, Conceptualization. **B. Vrancken:** Writing – review & editing, Visualization, Validation, Resources, Methodology, Data curation. **B. van Hooreweder:** Writing – review & editing, Visualization, Validation, Software, Formal analysis. **M.J. Mirzaali:** Writing – review & editing, Validation, Supervision, Resources, Project administration, Methodology, Funding acquisition, Data curation, Conceptualization.

Declaration of competing interest

The authors declare that they have no known competing financial interests or personal relationships that could have appeared to influence the work reported in this paper.

Data availability

Data will be made available on request.

References

[1] M.J. Mirzaali, A. Herranz de la Nava, D. Gunashekar, M. Nouri-Goushki, E. L. Doubrovski, A.A. Zadpoor, Fracture behavior of bio-inspired functionally graded soft–hard composites made by multi-material 3D printing: the case of colinear cracks, Materials 12 (17) (2019) 2735.

[2] M.J. Mirzaali, M.E. Edens, A.H. de la Nava, S. Janbaz, P. Vena, E.L. Doubrovski, A. A. Zadpoor, Length-scale dependency of biomimetic hard-soft composites, Scientific Reports 8 (1) (2018) 12052.

[3] M.J. Mirzaali, V. Mussi, P. Vena, F. Libonati, L. Vergani, M. Strano, Mimicking the loading adaptation of bone microstructure with aluminum foams, Materials & Design 126 (2017) 207–218.

[4] K. Gupta, K. Meena, Artificial bone scaffolds and bone joints by additive manufacturing: A review, Bioprinting 31 (2023) e00268.

[5] A. Benady, S.J. Meyer, E. Golden, S. Dadia, G.K. Levy, Patient-specific Ti-6Al-4V lattice implants for critical-sized load-bearing bone defects reconstruction, Materials & Design 226 (2023) 111605.

[6] H. Wang, Y. Wan, F. Meng, G. Zhao, X. Liu, S. Zhang, W. Su, Precise design, preparation, and biomechanical evaluation of customized additively manufactured Ti6Al4V porous fusion cage, Journal of Materials Research and Technology 33 (2024) 8198–8210.

[7] M. Kouhi, I.J. de Souza Araújo, F. Asa'ad, L. Zeenat, S.S.R. Bojedla, F. Pati, A. Zolfagharian, D.C. Watts, M.C. Bottino, M. Bodaghi, Recent advances in additive manufacturing of patient-specific devices for dental and maxillofacial rehabilitation, Dental Materials (2024).

[8] S. Ahmadi, G. Campoli, S.A. Yavari, B. Sajadi, R. Wauthlé, J. Schrooten, H. Weinans, A. Zadpoor, Mechanical behavior of regular open-cell porous

[9] biomaterials made of diamond lattice unit cells, Journal of the mechanical behavior of biomedical materials 34 (2014) 106–115.

[9] C. Gomez, A. Shoufandeh, W. Sun, Unit-cell based design and modeling in tissue engineering applications, Computer-Aided Design and Applications 4 (5) (2007).

[10] G. Ryan, P. McGarry, A. Pandit, D. Apatsidis, Analysis of the mechanical behavior of a titanium scaffold with a repeating unit-cell substructure, Journal of Biomedical Materials Research Part B: Applied Biomaterials: An Official Journal of The Society for Biomaterials, The Japanese Society for Biomaterials, and The Australian Society for Biomaterials and the Korean Society for Biomaterials 90 (2) (2009) 894–906.

[11] R. Nandhakumar, K. Venkatesan, A process parameters review on Selective laser melting-based additive manufacturing of Single and Multi-Material: Microstructure, Properties, and machinability aspects, Materials Today Communications 105538 (2023).

[12] S.R. Narasimharaju, W. Zeng, T.L. See, Z. Zhu, P. Scott, X. Jiang, S. Lou, A comprehensive review on laser powder bed fusion of steels: Processing, microstructure, defects and control methods, mechanical properties, current challenges and future trends, Journal of Manufacturing Processes 75 (2022) 375–414.

[13] M. Alaña, A. Cutolo, G. Probst, S.R. de Galarreta, B. Van Hooreweder, Understanding elastic anisotropy in diamond based lattice structures produced by laser powder bed fusion: Effect of manufacturing deviations, Materials & Design 195 (2020) 108971.

[14] G. Meyer, F. Brenne, T. Niendorf, C. Mittelstedt, Influence of the miniaturisation effect on the effective stiffness of lattice structures in additive manufacturing, Metals 10 (11) (2020) 1442.

[15] J. Pegues, S. Shao, N. Shamsaei, N. Sanaei, A. Fatemi, D. Warner, P. Li, N. Phan, Fatigue of additive manufactured Ti-6Al-4V, Part I: The effects of powder feedstock, manufacturing, and post-process conditions on the resulting microstructure and defects, International Journal of Fatigue 132 (2020) 105358.

[16] H. Dobbs, J. Robertson, Alloys for orthopaedic implant use, Engineering in Medicine 11 (4) (1982) 175–182.

[17] S.V. Muley, A.N. Vidvans, G.P. Chaudhari, S. Udainiya, An assessment of ultra fine grained 316L stainless steel for implant applications, Acta biomaterialia 30 (2016) 408–419.

[18] E. Wycisk, S. Siddique, D. Herzog, F. Walther, C. Emmelmann, Fatigue performance of laser additive manufactured Ti–6Al–4V in very high cycle fatigue regime up to 109 cycles, Frontiers in Materials 2 (2015) 72.

[19] S. Leuders, M. Thöne, A. Riemer, T. Niendorf, T. Tröster, H.a. Richard, H. Maier, On the mechanical behaviour of titanium alloy TiAl6V4 manufactured by selective laser melting: Fatigue resistance and crack growth performance, International journal of fatigue 48 (2013) 300–307.

[20] Z. Jia, L. Wang, 3D printing of biomimetic composites with improved fracture toughness, Acta Materialia 173 (2019) 61–73.

[21] A. Saroj, K.A. Jesna Rose, C.O. Arun, S. Anup, Design of a bio-inspired composite using probabilistic fracture mechanics, Journal of the Mechanical Behavior of Biomedical Materials 95 (2019) 96–102.

[22] G.X. Gu, L. Dimas, Z. Qin, M.J. Buehler, Optimization of composite fracture properties: method, validation, and applications, Journal of Applied Mechanics 83 (7) (2016).

[23] A.R. Balachandramurthi, J. Moverare, N. Dixit, R. Pederson, Influence of defects and as-built surface roughness on fatigue properties of additively manufactured Alloy 718, Materials Science and Engineering: A 735 (2018) 463–474.

[24] A. Du Plessis, S. Beretta, Killer notches: The effect of as-built surface roughness on fatigue failure in AlSi10Mg produced by laser powder bed fusion, Additive Manufacturing 35 (2020) 101424.

[25] C.N. Kelly, N.T. Evans, C.W. Irvin, S.C. Chapman, K. Gall, D.L. Safranski, The effect of surface topography and porosity on the tensile fatigue of 3D printed Ti-6Al-4V fabricated by selective laser melting, Materials Science and Engineering: C 98 (2019) 726–736.

[26] E. Wycisk, A. Solbach, S. Siddique, D. Herzog, F. Walther, C. Emmelmann, Effects of defects in laser additive manufactured Ti-6Al-4V on fatigue properties, Physics Procedia 56 (2014) 371–378.

[27] J. Günther, D. Krewerth, T. Lippmann, S. Leuders, T. Tröster, A. Weidner, H. Biermann, T. Niendorf, Fatigue life of additively manufactured Ti–6Al–4V in the very high cycle fatigue regime, International Journal of Fatigue 94 (2017) 236–245.

[28] P. Edwards, M. Ramulu, Fatigue performance evaluation of selective laser melted Ti–6Al–4V, Materials Science and Engineering: A 598 (2014) 327–337.

[29] S. Tammas-Williams, P.J. Withers, I. Todd, P.B. Prangnell, The influence of porosity on fatigue crack initiation in additively manufactured titanium components, Scientific reports 7 (1) (2017) 7308.

[30] C. Rodrigo, S. Xu, Y. Durandet, P. Tran, D. Ruan, Mechanical response of functionally graded lattices with different density grading strategies, Thin-Walled Structures 192 (2023) 111132.

[31] Y. Li, D. Jiang, R. Zhao, X. Wang, L. Wang, L.C. Zhang, High mechanical performance of lattice structures fabricated by additive manufacturing, Metals (2024).

[32] L. Xiao, W. Song, Additively-manufactured functionally graded Ti-6Al-4V lattice structures with high strength under static and dynamic loading: Experiments, International Journal of Impact Engineering 111 (2018) 255–272.

[33] R. Alkentar, N. Kladovasilakis, D. Tzetzis, T. Mankovits, Effects of pore size parameters of titanium additively manufactured lattice structures on the osseointegration process in orthopedic applications: a comprehensive review, Crystals 13 (1) (2023) 113.

[34] Y. Sun, Y. Wang, B. Dong, P. Yang, C. Ji, Y. Li, J. Ma, X. Ma, Understanding the relationship between pore structure and properties of triply periodic minimal

surface bone scaffolds, Journal of Materials Science: Materials in Medicine 36 (1) (2025) 1–19.

[35] B. Yadav, A. Alfantazi, A.A. Alazemi, A. Mandal, P.-C. Lin, P.-C. Huang, D.-Y. Yeh, D.-S. Liu, Microstructural and mechanical properties study of various lattice structures of SS316L-CNTs nano composites fabricated through additive manufacturing, Journal of Physics D: Applied Physics 58 (6) (2024) 065501.

[36] J. Peloquin, Y. Han, K. Gall, Printability and mechanical behavior as a function of base material, structure, and a wide range of porosities for polymer lattice structures fabricated by vat-based 3D printing, Additive Manufacturing 78 (2023) 103892.

[37] M. Arsentev, E. Topalov, S. Balabanov, E. Sysoev, I. Shulga, M. Akhmatnabiev, M. Sychov, E. Skorb, M. Nosonovsky, Crystal-inspired cellular metamaterials and triply periodic minimal surfaces, Biomimetics 9 (5) (2024) 285.

[38] L. Tian, B. Sun, X. Yan, A. Sharf, C. Tu, L. Lu, Continuous transitions of triply periodic minimal surfaces, Additive Manufacturing 84 (2024) 104105.

[39] D. Hoffman, Some basic facts, old and new, about triply periodic embedded minimal surfaces, Le Journal de Physique Colloques 51(C7) (1990) C7–197-C7-208.

[40] R. Hedayati, S. Janbaz, M. Sadighi, M. Mohammadi-Aghdam, A. Zadpoor, How does tissue regeneration influence the mechanical behavior of additively manufactured porous biomaterials? Journal of the mechanical behavior of biomedical materials 65 (2017) 831–841.

[41] S.A. Yavari, S. Ahmadi, R. Wauthle, B. Pouran, J. Schrooten, H. Weinans, A. Zadpoor, Relationship between unit cell type and porosity and the fatigue behavior of selective laser melted meta-biomaterials, Journal of the mechanical behavior of biomedical materials 43 (2015) 91–100.